

ARTICLE OPEN



Scalable and low-cost fabrication of flexible WS₂ photodetectors on polycarbonate

Jorge Quereda¹✉, Sruthi Kuriakose², Carmen Munuera¹ , Federico J. Mompean², Abdullah M. Al-Enizi³, Ayman Nafady³, Enrique Diez¹ , Riccardo Frisenda² and Andres Castellanos-Gomez¹ ✉

We present a low-cost and easy-to-implement technique to fabricate large-area WS₂ photodetector devices onto transparent and flexible polycarbonate substrates. The method relies on the deposition of large-area (in the cm scale) thin films (~30 nm thick) of WS₂ by a recently introduced abrasion-induced method. Interdigitated electrical contacts are then deposited by thermal evaporation through a shadow mask. The photodetectors present well-balanced performances with an good trade-off between responsivity (up to 144 mA/W at a source-drain voltage of 10 V and illumination power of 1 μW) and response time (down to ~70 μs) and a detectivity value of 10⁸ Jones. We found that the devices perform very reversibly upon several illumination and straining cycles and we found a moderate device-to-device variation.

npj Flexible Electronics (2022)6:23; <https://doi.org/10.1038/s41528-022-00157-9>

INTRODUCTION

Semiconducting transition metal dichalcogenides have attracted the interest of the materials science community since their recent application as field effect transistors and photodetectors^{1–6}. The outstanding combination of mechanical, optical and electrical properties, and their environmental stability, has motivated the integration of this family of semiconductors on flexible substrates for optoelectronic devices⁷. To date, many of the studied photodetector devices are based on mechanically exfoliated flakes^{8–10} and the experimental efforts towards improving the scalability are mostly focused on the synthesis of large-area transition metal dichalcogenides by chemical vapor deposition^{11–15} or by inkjet printing liquid-phase exfoliated materials^{16–19}. While chemical vapor deposition (CVD) provides a route to obtain high-performing devices on flexible substrates, its cost and fabrication complexity is much higher than that of inkjet printing. Nonetheless, inkjet printed devices (although less costly and complex than CVD-based ones) demonstrated lower performances so far. There is, thus, a need for exploring alternative approaches capable of yielding low-cost yet high-performing scalable photodetector materials based on transition metal dichalcogenides.

In this work, we fabricate WS₂ photodetectors on flexible and transparent polycarbonate substrates by an all-dry and inexpensive scalable deposition method: the abrasion-induced deposition. We demonstrate the parallel fabrication of many photodetectors with this low-tech deposition method. Interestingly, the fabricated photodetectors display responsivity values reaching 144 mA/W and fast response times of ~70 μs. Despite the simplicity and low cost of this fabrication method the devices are robust and they can be subjected to many illumination and bending cycles, recovering their initial state. Moreover, they show a moderate device-to-device variability. We thus believe that this kind of technology can be an interesting alternative to scale up flexible devices based on transition metal dichalcogenides for applications where the need for low-cost of the final device exceeds the need of high performance (e.g., disposable electronics).

RESULTS

Device fabrication

Devices were fabricated onto 250 μm thick polycarbonate substrates of ~15 × 20 mm². We selected polycarbonate as our polymer substrate because of its remarkable resistance to abrasion, which prevents potential degradation (scratching) of the substrate surface during the deposition process²⁰. Moreover, we found that other polymer substrates available in our laboratory (polyethylene terephthalate, PET, and polypropylene, PP) present deep scratches in their surfaces, which can hamper the electrical conductivity of the evaporated metal electrodes (see Supplementary Note 1). The photosensitive WS₂ film of the device was deposited by directly rubbing WS₂ micronized powder against the polycarbonate substrate (Fig. 1a–c). An approximate volume of ~8 mm³ of WS₂ powder is placed onto the surface of the polycarbonate substrate and gently rubbed with a cotton swab. We use a handheld multimeter to monitor the quality of the film. We continue the rubbing process until we get a resistance of ~5–10 MΩ between two probes separated by 1 mm. At this point we stop and get rid of the non-adhered excess WS₂ powder by blow drying with nitrogen. We also found that transmittance measurements can be used to assess the average thickness of the film, providing a fast feedback method during the abrasion process (see Supplementary Note 2).

As a final step, Ti (5 nm)/Au (100 nm) electrodes were deposited with e-beam evaporation through a shadow mask, see Fig. 1d, e. A zoomed-in optical microscopy image of one of the fabricated WS₂ devices with evaporated interdigitated electrodes is shown in Fig. 1f. The use of shadow masks and e-beam evaporation of metals allows us to fabricate electrodes with well-defined shape and edges, improving the reproducibility of the resulting devices with respect to the previously reported devices with hand drawn electrodes^{21,22}. Further, it also facilitates to a large extent the parallel fabrication of several devices at once.

The morphology and chemical composition of the as-deposited WS₂ films were characterized by scanning electron microscopy

¹GISC, Departamento de Física de Materiales, Universidad Complutense de Madrid, Madrid, Spain. ²Materials Science Factory, Instituto de Ciencia de Materiales de Madrid (ICMM-CSIC), 28049 Madrid, Spain. ³Department of Chemistry, College of Science, King Saud University, Riyadh 11451, Saudi Arabia. ⁴Nanotechnology Group, USAL–Nanolab, Universidad de Salamanca, 37008 Salamanca, Spain. ✉email: jorquere@ucm.es; Andres.castellanos@csic.es

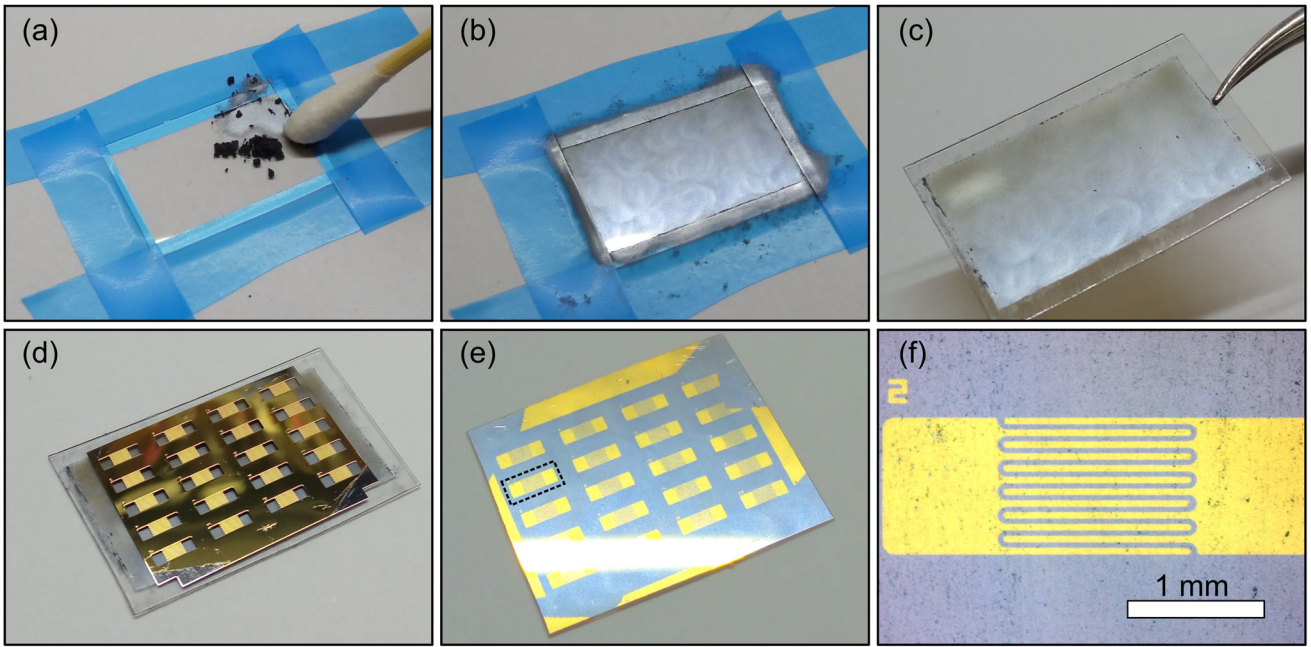


Fig. 1 Fabrication steps of the flexible large-area WS_2 photodetectors. **a** Fine WS_2 powder is rubbed against the surface of a polycarbonate substrate with a cotton swab. **b, c** Pictures of the WS_2 film on polycarbonate after deposition. **d** A shadow mask is placed onto the surface of the film. **e** Picture of a polycarbonate chip after the evaporation of 20 devices. **f** Higher magnification image of one of the devices, highlighted with a dashed rectangle in **e**.

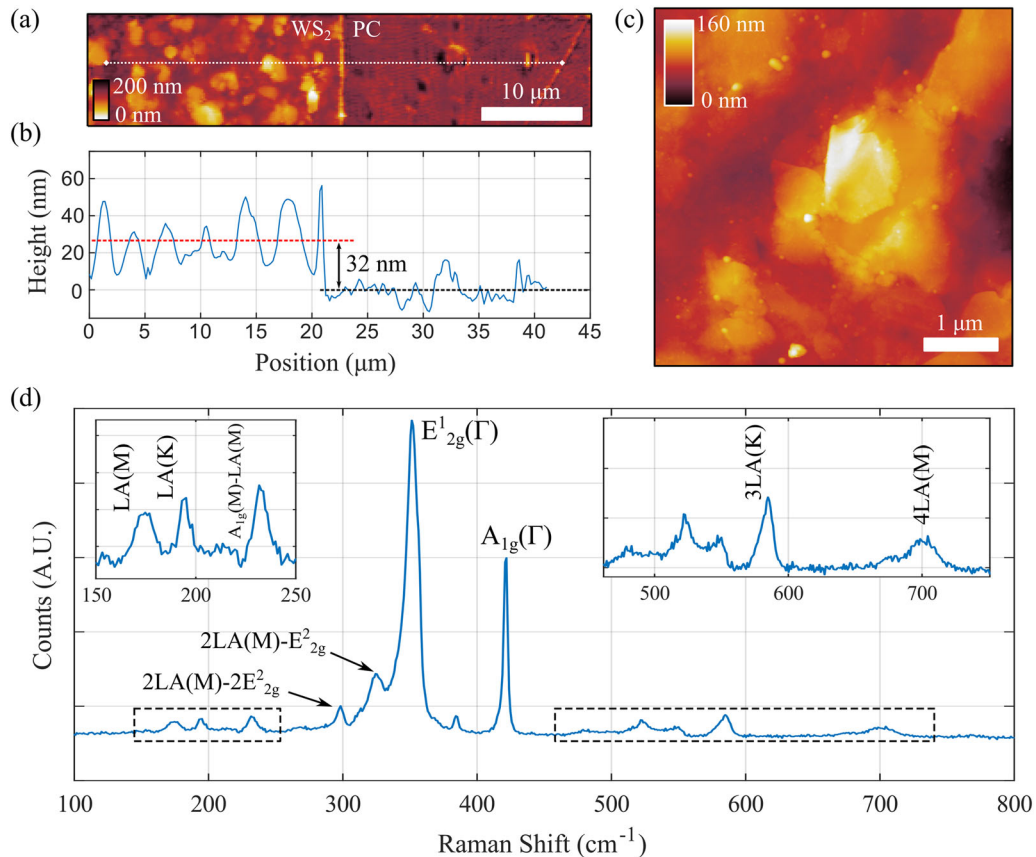


Fig. 2 Characterization of the as-deposited WS_2 film. **a** Atomic force microscopy image of the step between the WS_2 film and the bare polycarbonate substrate. **b** Line profile measured along the line in **a**. An average thickness of ~ 32 nm is estimated from the profile. **c** Higher magnification atomic force microscopy image of the WS_2 film where one can resolve some individual WS_2 flakes, parallel to the surface, within the film. **d** Raman spectrum of the WS_2 film. The main peaks associated with WS_2 are labeled in the figure.

(SEM), energy dispersive X-ray spectroscopy (EDX), atomic force microscopy (AFM) and Raman spectroscopy. We address the reader to Supplementary Note 3 for the SEM and EDX characterization of the device. We used AFM characterization to get quantitative information about the average thickness of the deposited film. Using a diamond-coated AFM tip we have microplowed part of the WS_2 film, leaving a region with bare polycarbonate (see Fig. 2a). We can then quantitatively measure the thickness of the film (Fig. 2b) that spans from 20 to 50 nm, with an average thickness of ~ 30 nm. While the thickness of the film cannot be accurately controlled during the abrasion deposition process, we find that, even between different batches, the fabricated films always present average thicknesses lower than 80 nm (see Supplementary Note 2). We attribute this to a friction reduction once a continuous film of WS_2 is achieved, which results in a decreasing abrasion between the surface and the rubbed van der Waals materials as the thickness increases, until the process does not allow for further material aggregation.

The AFM characterization also allowed us to get a deeper insight into the morphology of the WS_2 film. Figure 2c shows an AFM image acquired on one of the WS_2 films on polycarbonate where one can resolve the shape of individual WS_2 flakes, interconnected forming the film. From the AFM image one can also see how there is a large fraction of WS_2 flakes, laying flat, with their basal plane nearly parallel to the polycarbonate surface, indicating a preferential alignment of the flakes during the abrasion-induced deposition process. This is further confirmed by X-ray diffraction measurements, shown in Supplementary Note 4, where reflections from (00L) planes (with $L = 2, 4, 6, 8,$ and 10) were the most prominent in the diffraction pattern. Finally, we have also employed

Raman spectroscopy to characterize the level of crystallinity of the as-deposited WS_2 . Figure 2d shows a Raman spectrum measured on the WS_2 -covered polycarbonate substrate. The main spectral features of WS_2 can be clearly observed²³, indicating that the WS_2 crystals do not degrade during the device fabrication process. This is further confirmed by EDX measurements, shown in Supplementary Note 3. For comparison, a Raman spectrum acquired on the bare polycarbonate substrate is shown in Supplementary Note 5.

Performance of the WS_2 devices

Figure 3a shows the current vs. voltage (I s hereafter) characteristics of a WS_2 device in dark and upon illumination with a LED of 625 nm wavelength. Upon illumination the current across the device increases because of the extra photogenerated charge carriers in the channel. The difference between these two I s yield the photocurrent I_{ph} . Figure 3b shows a set of current vs. time (I - t hereafter) measurements. The light is turned ON between time = 2 s and time = 4 s, allowing to simultaneously determine the dark current, the current upon illumination and the response time of the device. Note that the device response is faster than the mechanical shutter used in this measurement, a quantitative characterization of the device response speed will be discussed below. The measurement has been repeated for increasing illumination power to study the power dependence of the photogenerated current and extract information about the photogeneration mechanism.

In 2D transition metal dichalcogenide photodetectors, photoresponse typically stems from two main mechanisms: The photoconductive effect and photogating effect^{24–30}. In the photoconductive effect, the illumination with photons of higher

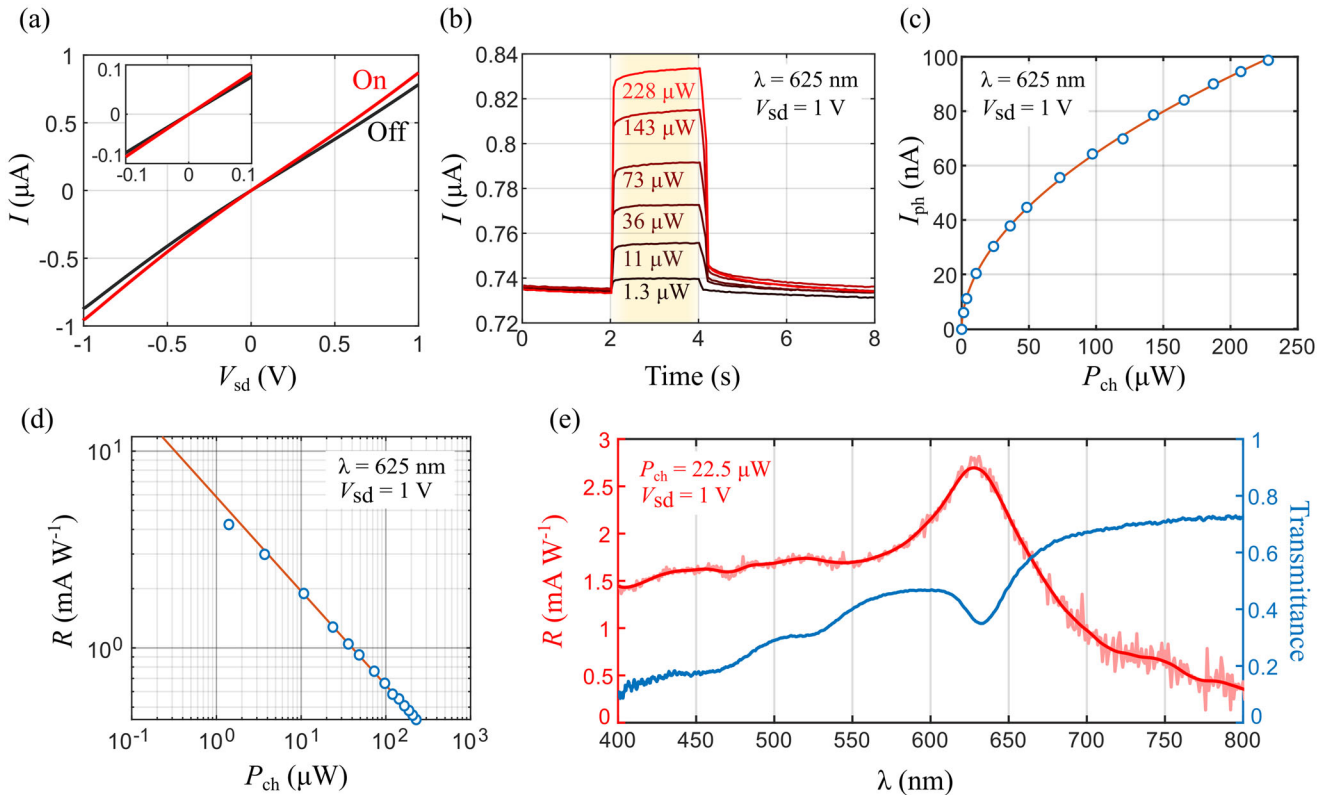


Fig. 3 Optoelectronic response of the devices. **a** I vs. V_{sd} characteristics of a WS_2 device, measured in the dark (black) and upon illumination (red) with wavelength $\lambda = 625$ nm and power $P = 228 \mu\text{W}$ (spot diameter $850 \mu\text{m}$). **b** Current vs. time measurements at $V_{sd} = 1$ V, acquired while turning the illumination on (at $t = 2$ s) and off (at $t = 4$ s) for $\lambda = 625$ nm and increasing values of illumination power, from 1.3 to $228 \mu\text{W}$. The sample is kept in dark for 20 s after each measurement cycle to allow for stabilization. **c** Power dependence of the photocurrent, I_{PC} , extracted from the on-off cycles shown in panel **b** as the difference between the current measured immediately before and one second after illumination is turned on. The orange line is a fitting to a power law $I_{PC} \propto P^a$, with $a \approx 0.5$. **d** Device photoresponsivity as a function of the illumination power for $\lambda = 625$ nm and $V_{sd} = 1$ V. **e** Typical spectral dependence of the photoresponsivity (red line, left axis) and optical transmittance (blue, right axis) of the WS_2 devices.

energy than the semiconductor band-gap excites an electron from the valence band to the conduction band forming an electron–hole pair that, upon a bias voltage applied along the channel, can be separated leading to an increased charge carrier density and electrical conductivity. Therefore, the photocurrent generated by this mechanism is typically proportional to the incident light power as the number of excited electrons is linearly proportional to the incident photons. The photogating effect^{27,31} is a special case of photoconductive mechanism that occurs in semiconducting materials with defect states that can trap the photogenerated minority charge carriers. The accumulation of trapped charges in the channel lead to a shift of the Fermi energy of the semiconducting material through the electric field effect modifying the conductance of the device. In the photogating case, for sufficiently high illumination intensity the minority charge carriers traps can become filled-in, and thus, photocurrent cannot increase linearly proportional to the illumination power leading to a typical sub-linear power dependence. Figure 3c summarizes the extracted photocurrent values, obtained from the I - t measurements upon different illumination power values. The photocurrent follows a sub-linear trend that can be fitted to a power law $I_{PC} \propto P_{ch}^{\alpha}$ with $\alpha \approx 0.5$, as expected for photogating-dominated photoresponse. From the photocurrent measurements one can also determine the responsivity (R), one of the most important figures-of-merit of photodetectors that allows for direct comparison of performance of different devices. The responsivity (R) is defined as:

$$R = \frac{I_{PC}}{P_{ch}} \quad (1)$$

where I_{PC} is the photocurrent and P_{ch} the light power reaching the semiconducting WS_2 channel. Figure 3d displays the extracted responsivity values for different incident powers. Note that, due to the sub-linear power dependence of I_{PC} , the responsivity decreases for increasing illumination power. At low-illumination powers, the device reaches a remarkable responsivity value of up to 4 mA/W. We have measured higher responsivity values for devices operated at larger bias voltage ($V_{ds} = 10$ V), reaching ~ 144 mA/W for low-illumination power densities (shown in Supplementary Note 6). Figure 3e shows the device responsivity as a function of the illumination wavelength for a fixed illumination power 22.5 μ W and a bias voltage of 1 V (measurement procedure described in Supplementary Note 7). The responsivity spectrum displays a prominent peak at ~ 630 nm and two weaker peak features ~ 450 nm ~ 520 nm that are in agreement with the dips observed in the transmittance spectra, attributed to direct valence-to-conduction band transitions accompanied with the generation of tightly bound excitons. At longer wavelength, beyond the ~ 630 nm peak (labeled as A exciton peak, according to the literature), the responsivity drops monotonically. Nonetheless, the device still displays a sizeable responsivity in the near-infrared spectroscopy (NIR) region up to 800 nm. This photoresponse is most probably due to phonon-assisted indirect optical transitions, as well as optical absorption by localized states within the band-gap.

To further investigate the performance of the WS_2 on polycarbonate photodetectors we have quantitatively characterized their maximum detection speed. We illuminate the device with a solid-state laser diode (660 nm of wavelength). The laser controller allows us to modulate it with a square-wave signal with frequency ranging from DC to 150 kHz. We connect the device to a lock-in amplifier (Zurich Instruments, MFLI DC-500 kHz) to measure the spectrum of the device current in the frequency domain (Fig. 4a). Figure 4b shows two of these spectra: one when the device is in the dark state (black) and another one when the device is excited with the laser diode modulated with a square wave of 33 kHz (red). Upon illumination with the modulated laser, the current spectra show a sharp peak at the modulation frequency. By measuring the intensity of that peak as a function of the modulation frequency we can build-up a plot of the frequency response of the device. Figure 4c shows the intensity of the peak at the modulation frequency, normalized at the value measured at the lowest frequency, as a function of the modulation frequency. At low-frequency the response of the device remains rather constant and it starts to drop at 1–2 kHz. The cut-off frequency (f_{3dB}) is

defined as the point where the device response drops by -3 dB, which corresponds to 5 kHz. The response time (τ) of the device can be estimated as $\tau \approx 0.35/f_{3dB}$, giving ~ 70 μ s.

Table 1 compares the maximum responsivity and the minimum response times reported in the literature for different large-area flexible photodetectors, particularly focusing on those based on van der Waals materials. Our abrasion-deposited WS_2 photodetector on polycarbonate has a good combination between high responsivity (up to 144 mA/W) and remarkably low-response time (~ 70 μ s). Only devices fabricated with CVD-grown WS_2 achieve similar balance between high response and fast operation^{32–34}. Nonetheless, these CVD-based devices result more expensive and require a sophisticated method to transfer the grown WS_2 film to the final flexible substrate, making more difficult its implementation. Among the lower cost deposition methods, liquid-phase exfoliation-based deposition and electrophoresis provide devices with responsivities spanning from 10^{-5} to 800 mA/W and response times in the 0.01 s to 2 s^{19,35–40}. Other low-cost deposition methods to fabricate large-area photodetectors, like sputtering deposition or hydrothermal synthesis, yields responsivities in the 0.02 to 5 mA/W and response times that are even higher than those of devices based on liquid-phase exfoliated sensing material. Solution processed photodetectors, integrating hybrid inorganic-organic perovskites, have demonstrated very high responsivity values (up to 10^9 A/W) but with slower response (in the 0.02 s to 50 s)^{18,41}. WS_2 devices on PET, fabricated with a similar abrasion deposition method but employing transferred CVD-grown graphene electrodes, reported responsivities up to 24 mA/W but with response times in the ~ 10 s range. We thus stress that our abrasion-deposited WS_2 photodetector on polycarbonate with evaporated interdigitated gold electrodes present a well-balanced performance that will be highly desirable for applications requiring a fast response time like image acquisition.

We have also experimentally determined the detectivity (D^*) following the guidelines drafted by Paul Meredith, Jinsong Huang and co-workers in ref. 42 that explain the good practices for the characterization of photodetectors based on nanomaterials. Briefly, the device is illuminated with pulsed light (a fiber-coupled LED modulated with a square-wave signal in our case) at 1 Hz and a long I - t sequence is measured. Then the measured data is Fourier transformed and the amplitude of the peak corresponding to the modulation at 1 Hz is extracted (Fig. 4d). The measurement is repeated with lower and lower illumination intensity until the 1 Hz peak in the FFT becomes undistinguishable from the background noise. Figure 4e shows several current frequency spectra where a prominent peak at the modulation frequency, 1 Hz, can be observed. Figure 4f summarizes the measured signal-to-noise ratio for different illumination powers. We found that for a light power of 7.8 nW, the peak at 1 Hz in the frequency spectrum has a height comparable with the noise-floor. That provides a quantitative measurement of the noise equivalent power (NEP) of the device, a magnitude that can help to determine the detectivity. In fact, the detectivity (D^*) is defined as:

$$D^* = \frac{\sqrt{A B}}{NEP} \quad (2)$$

where A is the area of the device and B is the bandwidth. Using area 0.001 cm^2 and bandwidth 5 kHz we get $D^* = 10^8$ Jones.

Device stability and reproducibility

The robustness and reproducibility of the WS_2 photodetector devices is firstly tested by measuring 200 cycles of OFF/ON/OFF illumination (Fig. 5a). During this measurement the drift is minimal ($\sim 0.25\%$ per minute) and one can observe how the device reproducibly switches between the dark and illuminated state (Fig. 5b). We have included a histogram besides the I - t trace to quantify the low-variability of the switching.

In order to test the resilience to mechanical deformations we have fabricated a cantilever-shaped polycarbonate strip with WS_2 photodetectors on its surface. Then the cantilever was clamped at one end and a magnet was glued at the free-end. Using a linear

motor stage equipped with another permanent magnet we could subject the polycarbonate cantilever to cycles of deformation (Fig. 6a, b). We measured the current ($V_{ds} = 1$ V) flowing through one of the WS_2 devices located close to the clamping point (Fig. 6c). We calculated a maximum strain value upon cantilever deflection of $\sim 0.7\%$ ⁴³ (Discussed in Supplementary Note 8). The current flowing through the device strongly varies upon mechanical deformation: from ~ 90 nA for the unstrained situation to ~ 0.2 nA upon uniaxial strain of 0.7%. We attribute this strong dependence of the current upon uniaxial strain to the percolative nature of the electrical conduction in this system. The WS_2 film is composed of a network of interconnected flakes and the uniaxial tension can cause the flakes to slide, reducing the effective inter-flake hopping and thus leading to a drop in current. Remarkably, the devices recover the initial current state once the uniaxial strain is released. Figure 6d shows a histogram of the current, extracted from the I vs t curve, where a small variability of the current in the unstrained and strained states is observed.

To further characterize the robustness of the devices fabricated with this method, we have measured a total of 15 devices. Figure 7a, b show the dark current (at $V_{ds} = 1$ V) and photocurrent (at $\lambda = 625$ nm and $P_{ch} = 230$ μ W) of the devices. The dark current spans from 0.7 to 3.6 μ A, clustering around 1 μ A. The photocurrent spans from 90 nA to 320 nA, clustering around 120 μ A. Given the

percolative nature of the abrasion-deposited film, which is constituted by an ensemble of interconnected flakes, fluctuations of the film resistance are to be expected. Note that, as discussed above (see Fig. 6) the drain-source current of the device is extremely sensitive to the flake-to-flake hopping strength. Thus, the fact that I_0 remains within the same order of magnitude for all the measured devices (and even for different batches; see Supplementary Note 9) seems to indicate that the degree of percolation between flakes is rather uniform within the samples.

Interestingly, the ratio between the photocurrent and the dark current presents even lower dispersion, spanning only between 0.09 and 0.19 (Fig. 7c). Moreover, the exponent of the power-dependent photocurrent, α , remains remarkably constant and near to 0.5 for the 15 studied devices. This seem to indicate a very similar density of minority charge carrier traps in all the studied samples.

DISCUSSION

In summary, we have demonstrated a low-cost and easy-to-implement method to fabricate large-area WS_2 photodetector devices onto transparent and flexible polycarbonate substrates. The method is based on the deposition of a large-area of ~ 30 nm thick WS_2 by abrasion-induced deposition. The as-fabricated

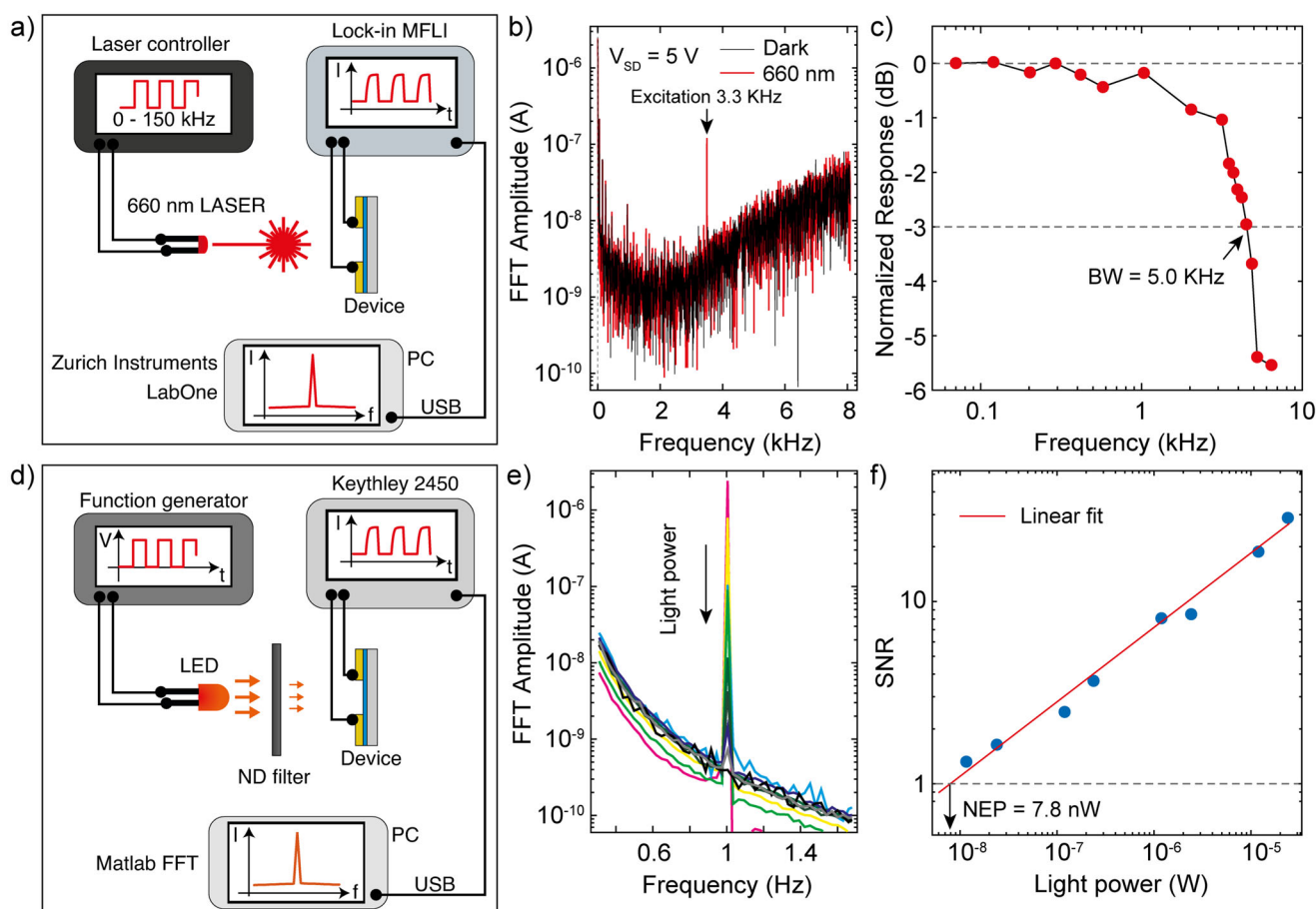


Fig. 4 AC and small signal response of the devices. **a** Schematic representation of the experimental configuration to measure the bandwidth of the device. **b** Fast Fourier transforms of the current versus time recorded in a WS_2 device in dark (black) and under 660 nm illumination modulated through a 3.3 KHz square wave. The peak at 3.3 KHz corresponds to the response of the device. **c** Frequency plot of the AC response of the device normalized to the DC response (under continuous illumination) in dB. **d** Schematic representation of the experimental configuration to measure the detectivity of the device. **e** Fast Fourier transforms of the current versus time recorded in a WS_2 device illuminated with a 660 nm LED modulated at 1 Hz and decreasing illumination powers. **f** Log-log representation of the signal-to-noise ratio of the 1 Hz peak from panel **e** versus incident illumination power. The cross between the linear fit and the SNR = 1 line gives the noise equivalent power (NEP).

Table 1. Summary of performances of different large-area flexible photodetectors in the literature.

Sensing material	Substrate	Deposition method	Max. responsivity (mA/W)	Min. response time (s)	Dark current (A)	Voltage (V)	Illumination power (mW/cm ²)	References
WS ₂	Polycarbonate	Abrasion	144	7·10 ⁻⁵	2·10 ⁻⁵	10	1	This work
WS ₂	Polyimide	RF sputtering	1.7	0.5	4·10 ⁻¹⁰ to 8·10 ⁻⁶	10	5 to 15	44
WS ₂	Polyimide	CVD + transfer	5	~0.12	2·10 ⁻¹³	10	0.1	32
WS ₂	Filter membrane	Hydrothermal	4	8 to 12	8·10 ⁻⁸	5	10	45
WS ₂	Parylene	CVD + transfer	5·10 ⁶	<2·10 ⁻³	10 ⁻¹² to 10 ⁻⁴	5	0.03 to 30	33
WS ₂	PET	Abrasion	24	12	N/A	N/A	50	22
WS ₂	PET	Liquid-phase exfoliation	>1	~0.5	2·10 ⁻⁶	1	7 mW ^a	35
WS ₂ /graphene	Cellulose paper	Electrophoresis	400	2	1.5·10 ⁻⁴	10	0.6	36
WSe ₂ nanodots	Filter paper	Liquid-phase exfoliation	800	0.7	2·10 ⁻⁵	20	1	37
WSe ₂ /MoS ₂	Standard paper	Liquid-phase exfoliation	124	~0.5	10 ⁻⁸	1	0.1	38
MoS ₂	Standard paper	Abrasion	0.001	~10	7·10 ⁻⁸	20	10 to 100	21
MoS ₂	Polyimide	Liquid-phase exfoliation	50	0.01	10 ⁻⁶	10	20 to 2000	19
MoS ₂	PEN	CVD + transfer	20	2	2·10 ⁻⁹	10	5	16
MoS ₂ /graphene	Polyimide	Liquid-phase exfoliation	300	N/A	N/A	20	5	39
MoS ₂ /graphene	PET	CVD + transfer	~4500	N/A	6·10 ⁻⁶ to 7.5·10 ⁻⁵	0.1	100 μW ^a	34
MoS ₂ /ZnS	Cellulose paper	Hydrothermal	0.018	~50	5·10 ⁻⁷	1	20	46
MoSe ₂	Technical paper (PEL P60)	Liquid-phase exfoliation	~5·10 ⁻⁴	N/A	N/A	N/A	N/A	40
MoTe ₂			~2·10 ⁻³		N/A	N/A	N/A	
WS ₂			~1·10 ⁻⁴		N/A	N/A	N/A	
MoS ₂			~7·10 ⁻⁵		10 ⁻⁹	5	30 μW ^a	47
Graphene/CNT	PET	Spincoating + CVD + transfer	~5·10 ⁴	~0.04 to 0.06	7·10 ⁻⁶	0.01	0.5 μW ^a	
PEDOT:PPS/perovskite	Polyimide	Solution process	~1·10 ¹²	~50	N/A	N/A	0.015	41
Layered perovskite	Polyimide	Solution process	170	0.02	2·10 ⁻¹¹	40	0.6	18

^aReference do not provide enough information to extract the power density.

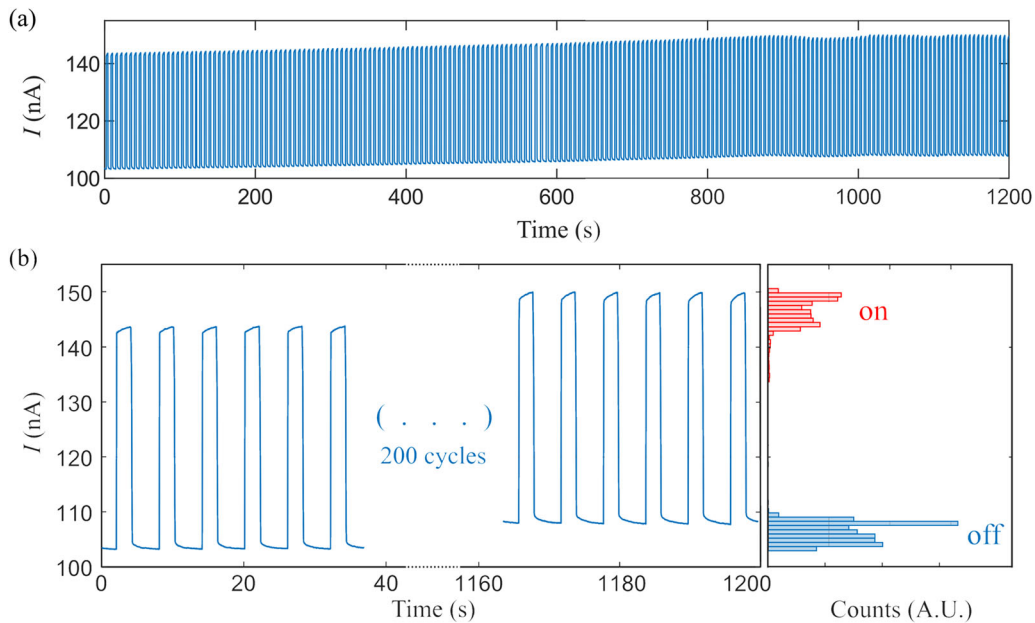


Fig. 5 Stability of the WS₂ devices. **a** I - t measurement cycles in the WS₂ device while alternatively switching the illumination on and off during a 20-min period. **b** Zoom-in of the initial and final sections of **a**. The right panel in **b** shows a histogram of the measured current I over the complete 20-min interval.

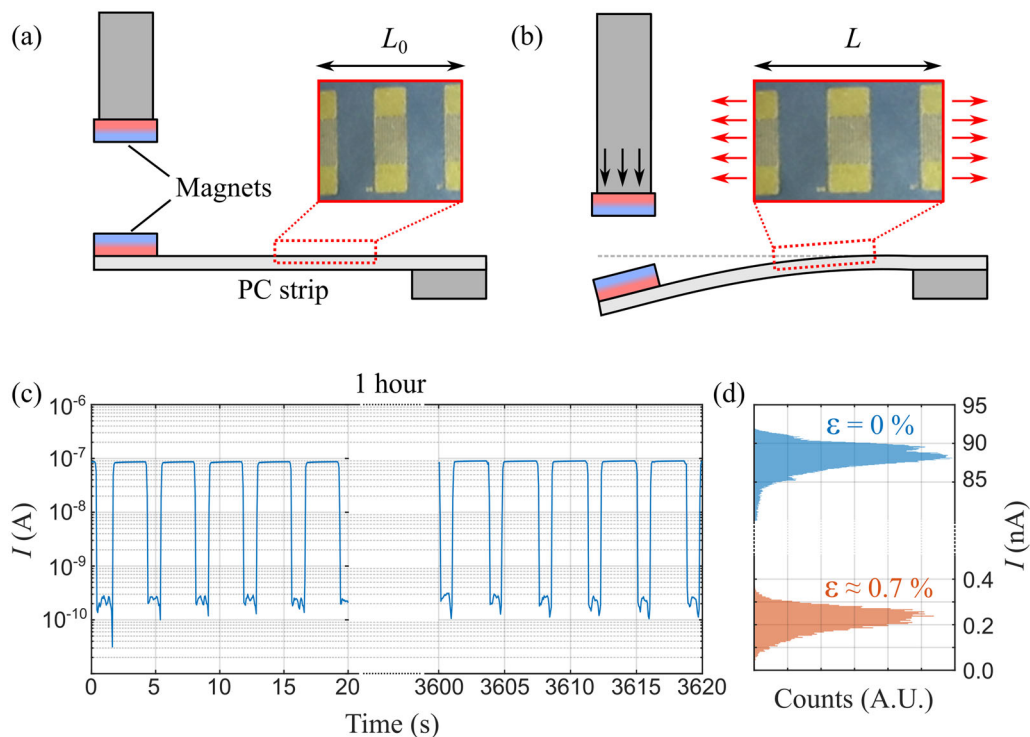


Fig. 6 Mechanical resilience of the WS₂ devices. **a, b** Schematic depiction of the experimental configuration with the linear motor stage retracted (**a**) and extended (**b**). Upon extension of the linear stage, the surface of the PC strip elongates uniaxially by $\sim 0.7\%$. **c** I - t measurement cycles in the WS₂ device, measured at $V_{sd} = 1$ V while periodically extending and retracting the linear stage. **d** Histogram of the registered current I during 1 h of measurement.

devices were characterized by SEM, EDX, AFM, and Raman spectroscopy. We thoroughly studied their performance as photodetectors in the VIS–NIR range of the spectrum finding a good trade-off between responsivity (up to 144 mA/W) and response time (down to ~ 70 μ s) and a detectivity value of 10^8 Jones. The devices performance was very reversible upon illumination and deformation cycles and we found a relatively

low (taking into account the percolation nature of the WS₂ film) device-to-device variation. We believe that our results demonstrate the feasibility of this kind of devices in certain applications requiring a good balance between low-cost/low-tech fabrication and good optoelectronic performance. The results presented here are very general and could be reproduced with other van der Waals materials, opening a wide field of research.

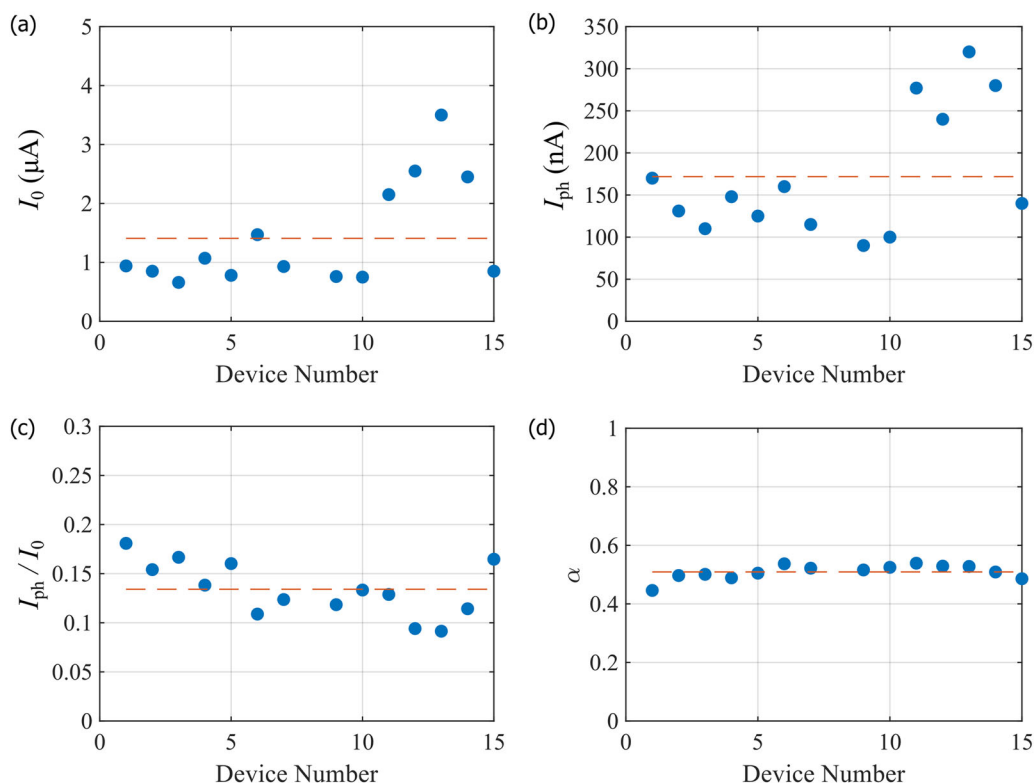


Fig. 7 Reproducibility of the devices. “Dark” current I_0 (a) and photocurrent I_{PC} (b) registered in 15 different devices. c Ratio between I_{PC} and I_0 . d α coefficient extracted from fitting the power dependence of I_{PC} to $I_{PC} \propto P^\alpha$. The orange, dashed lines in panels a–d represent average values over the full set of 15 devices.

METHODS

Materials

We used 250 μm thick sheets of polycarbonate purchased at Modulor (www.modulor.de, 27 €/m²). Other polymer substrates used for the Supplementary Material were also purchased at Modulor. WS₂ micronized powder was purchased at Alfa Aesar (ref. 11829.18, 99.8% purity). The shadow masks for the metal deposition were purchased at Ossila (ref. E323; channel length = 50 μm ; effective channel width = 18.23 mm).

Optoelectronic measurements

The photoresponse of the WS₂ devices is tested with a homebuilt probe station operating at room temperature in air. The system is connected to a Keithley 2450 source-measure unit to measure the electrical transport. For the optical excitation we recur to multimode fiber-coupled light sources, attached to the optical inspection system. This allows us to produce a circular spot of 850 μm in diameter with homogeneous power density over the sample. We employed 17 LED sources (Thorlabs, MxxxFy series) of different wavelengths to study the power-dependent photocurrent generation, a 660 nm solid-state laser diode (OF-20B-660-(5-30)-G, from OEABT) to determine the device response speed and a Xenon lamp with an integrated monochromator (Bentham TLS120Xe) to test the photoresponse at different illumination conditions.

DATA AVAILABILITY

The data that supports the findings of this study are available from the corresponding author upon request.

CODE AVAILABILITY

Code sharing not applicable to this manuscript.

Received: 1 October 2021; Accepted: 20 March 2022;
Published online: 21 April 2022

REFERENCES

- Jariwala, D., Sangwan, V. K., Lauhon, L. J., Marks, T. J. & Hersam, M. C. Emerging device applications for semiconducting two-dimensional transition metal dichalcogenides. *ACS Nano* **8**, 1102–1120 (2014).
- Wang, Q. H., Kalantar-Zadeh, K., Kis, A., Coleman, J. N. & Strano, M. S. Electronics and optoelectronics of two-dimensional transition metal dichalcogenides. *Nat. Nanotechnol.* **7**, 699–712 (2012).
- Castellanos-Gomez, A. Why all the fuss about 2D semiconductors? *Nat. Photon.* **10**, 202–204 (2016).
- Xia, F., Wang, H., Xiao, D., Dubey, M. & Ramasubramanian, A. Two-dimensional material nanophotonics. *Nat. Photon.* **8**, 899–907 (2014).
- Koppens, F. H. L. et al. Photodetectors based on graphene, other two-dimensional materials and hybrid systems. *Nat. Nanotechnol.* **9**, 780–793 (2014).
- Fiori, G. et al. Electronics based on two-dimensional materials. *Nat. Nanotechnol.* **9**, 768–779 (2014).
- Akinwande, D., Petrone, N. & Hone, J. Two-dimensional flexible nanoelectronics. *Nat. Commun.* **5**, 5678 (2014).
- Chang, H.-Y. et al. High-performance, highly bendable MoS₂ transistors with high-K dielectrics for flexible low-power systems. *ACS Nano* **7**, 5446–5452 (2013).
- Yoo, G. et al. Flexible and wavelength-selective MoS₂ phototransistors with monolithically integrated transmission color filters. *Sci. Rep.* **7**, 40945 (2017).
- Gant, P. et al. A strain tunable single-layer MoS₂ photodetector. *Mater. Today* **27**, 8–13 (2019).
- Conti, S. et al. Low-voltage 2D materials-based printed field-effect transistors for integrated digital and analog electronics on paper. *Nat. Commun.* **11**, 3566 (2020).
- Xia, J. et al. CVD synthesis of large-area, highly crystalline MoSe₂ atomic layers on diverse substrates and application to photodetectors. *Nanoscale* **6**, 8949–8955 (2014).
- Sun, Z. et al. Infrared photodetectors based on CVD-grown graphene and PbS quantum dots with ultrahigh responsivity. *Adv. Mater.* **24**, 5878–5883 (2012).
- Lee, J. et al. 25 GHz embedded-gate graphene transistors with high-k dielectrics on extremely flexible plastic sheets. *ACS Nano* **7**, 7744–7750 (2013).
- Chang, H.-Y. et al. Large-area monolayer MoS₂ for flexible low-power RF nanoelectronics in the GHz regime. *Adv. Mater.* **28**, 1818–1823 (2016).
- Kim, T.-Y. et al. Transparent large-area MoS₂ phototransistors with inkjet-printed components on flexible platforms. *ACS Nano* **11**, 10273–10280 (2017).

17. Torrisi, F. et al. Inkjet-printed graphene electronics. *ACS Nano* **6**, 2992–3006 (2012).
18. Min, M., Hossain, R. F., Adhikari, N. & Kaul, A. B. Inkjet-printed organohalide 2D layered perovskites for high-speed photodetectors on flexible polyimide substrates. *ACS Appl. Mater. Interfaces* **12**, 10809–10819 (2020).
19. Seo, J.-W. T. et al. Fully inkjet-printed, mechanically flexible MoS₂ nanosheet photodetectors. *ACS Appl. Mater. Interfaces* **11**, 5675–5681 (2019).
20. Hozumi, A., Kato, Y. & Takai, O. Two-layer hard coatings on transparent resin substrates for improvement of abrasion resistance. *Surf. Coat. Technol.* **82**, 16–22 (1996).
21. Mazaheri, A., Lee, M., van der Zant, H. S. J., Frisenda, R. & Castellanos-Gomez, A. MoS₂-on-paper optoelectronics: drawing photo-detectors with van der Waals semiconductors beyond graphite. *Nanoscale* **12**, 19068–19074 (2020).
22. Nutting, D. et al. Heterostructures formed through abraded van der Waals materials. *Nat. Commun.* **11**, 3047 (2020).
23. Peimyo, N. et al. Thermal conductivity determination of suspended mono- and bilayer WS₂ by Raman spectroscopy. *Nano Res.* **8**, 1210–1221 (2015).
24. Furchi, M. M., Polyushkin, D. K., Pospischil, A. & Mueller, T. Mechanisms of photoconductivity in atomically thin MoS₂. *Nano Lett.* **14**, 6165–6170 (2014).
25. Miller, B., Parzinger, E., Vernickel, A., Holleitner, A. W. & Wurstbauer, U. Photogating of mono- and few-layer MoS₂. *Appl. Phys. Lett.* **106**, 1–5 (2015).
26. Island, J. O., Blanter, S. I., Buscema, M., van der Zant, H. S. J. & Castellanos-Gomez, A. Gate controlled photocurrent generation mechanisms in high-gain In 2 Se 3 phototransistors. *Nano Lett.* **15**, 7853–7858 (2015).
27. Fang, H. & Hu, W. Photogating in low dimensional photodetectors. *Adv. Sci.* **4**, 1700323 (2017).
28. Huang, H. et al. Highly sensitive visible to infrared MoTe₂ photodetectors enhanced by the photogating effect. *Nanotechnology* **27**, 445201 (2016).
29. Quereda, J., Ghiasi, T. S., van Zwol, F. A., van der Wal, C. H. & van Wees, B. J. Observation of bright and dark exciton transitions in monolayer MoSe₂ by photocurrent spectroscopy. *2D Mater.* **5**, 015004 (2018).
30. Kufer, D. & Konstantatos, G. Highly sensitive, encapsulated MoS₂ photodetector with gate controllable gain and speed. *Nano Lett.* **15**, 7307–7313 (2015).
31. Vaquero, D. et al. Fast response photogating in monolayer MoS₂ phototransistors. *Nanoscale* 16156–16163 <https://doi.org/10.1039/d1nr03896f> (2021).
32. Lan, C. et al. Wafer-scale synthesis of monolayer WS₂ for high-performance flexible photodetectors by enhanced chemical vapor deposition. *Nano Res.* **11**, 3371–3384 (2018).
33. Aji, A. S., Solís-Fernández, P., Ji, H. G., Fukuda, K. & Ago, H. High mobility WS₂ transistors realized by multilayer graphene electrodes and application to high responsivity flexible photodetectors. *Adv. Funct. Mater.* **27**, 1703448 (2017).
34. De Fazio, D. et al. High responsivity, large-area graphene/MoS₂ flexible photodetectors. *ACS Nano* **10**, 8252–8262 (2016).
35. McManus, D. et al. Water-based and biocompatible 2D crystal inks for all-inkjet-printed heterostructures. *Nat. Nanotechnol.* **12**, 343–350 (2017).
36. Pataniya, P. M. & Sumesh, C. K. WS₂ nanosheet/graphene heterostructures for paper-based flexible photodetectors. *ACS Appl. Nano Mater.* **3**, 6935–6944 (2020).
37. Pataniya, P. et al. Paper-based flexible photodetector functionalized by WSe₂ nanodots. *ACS Appl. Nano Mater.* **2**, 2758–2766 (2019).
38. Pataniya, P. M., Patel, V. & Sumesh, C. K. MoS₂/WSe₂ nanohybrids for flexible paper-based photodetectors. *Nanotechnology* **32**, 315709 (2021).
39. Hossain, R. F., Deaguero, I. G., Boland, T. & Kaul, A. B. Biocompatible, large-format, inkjet printed heterostructure MoS₂-graphene photodetectors on conformable substrates. *NPJ 2D Mater. Appl.* **1**, 28 (2017).
40. McManus, D. et al. Photocurrent study of all-printed photodetectors on paper made of different transition metal dichalcogenide nanosheets. *Flex. Print. Electron.* **3**, 034005 (2018).
41. Xie, C., You, P., Liu, Z., Li, L. & Yan, F. Ultrasensitive broadband phototransistors based on perovskite/organic-semiconductor vertical heterojunctions. *Light Sci. Appl.* **6**, e17023–e17023 (2017).
42. Fang, Y., Armin, A., Meredith, P. & Huang, J. Accurate characterization of next-generation thin-film photodetectors. *Nat. Photon.* **13**, 1–4 (2019).
43. Tsoukleri, G. et al. Subjecting a graphene monolayer to tension and compression. *Small* **5**, 2397–2402 (2009).
44. Kim, B. H., Yoon, H., Kwon, S. H., Kim, D. W. & Yoon, Y. J. Direct WS₂ photodetector fabrication on a flexible substrate. *Vacuum* **184**, 109950 (2021).
45. Li, J., Han, J., Li, H., Fan, X. & Huang, K. Large-area, flexible broadband photodetector based on WS₂ nanosheets films. *Mater. Sci. Semicond. Process.* **107**, 104804 (2020).
46. Gomathi, P. T., Sahatiya, P. & Badhulika, S. Large-area, flexible broadband photodetector based on ZnS-MoS₂ hybrid on paper substrate. *Adv. Funct. Mater.* **27**, 1701611 (2017).
47. Liu, Y. et al. Graphene-carbon nanotube hybrid films for high-performance flexible photodetectors. *Nano Res.* **10**, 1880–1887 (2017).

ACKNOWLEDGEMENTS

We thank Felix Carrascoso (ICMM-CSIC) for support with the metal evaporation. This work received funding from the European Research Council (ERC) under the European Union's Horizon 2020 research and innovation program (grant agreement no. 755655, ERC-StG 2017 project 2D-TOPSENSE), the Ministry of Science and Innovation (Spain) through the project PID2020-115566RB-I00. A.C.-G., A.M.A.-E., and A.N. extend their sincere appreciation to the Distinguished Scientist Fellowship Program (DSFP) at King Saud University for funding of this work. R.F. acknowledges the support from the Spanish Ministry of Economy, Industry, and Competitiveness (MINECO) through a Juan de la Cierva-formation fellowship 2017 FJCI-2017-32919. J. Q. and E.D. acknowledge financial support from the Agencia Estatal de Investigación of Spain (Grants PID2019-106820RB, RTI2018-097180-B-I00, and PGC2018-097018-B-I00) and the Junta de Castilla y León (Grants SA256P18 and SA121P20), including funding by ERDF/FEDER. J.Q. acknowledges financial support from Universidad Complutense de Madrid and European Commission (MSCA COFUND UNA4CAREER grant. Project number 4129252) and from MICINN (Spain) through the program Juan de la Cierva-Incorporación.

AUTHOR CONTRIBUTIONS

A.C.-G. and S.K. fabricated the samples. J.Q., S.K., C.M., F.J.M., R.F., and A.C.-G. performed the characterization of the films. J.Q. performed the measurements of the devices with support and supervision of R.F., E.D., and A.C.-G. J.Q., S.K., C.M., A.M.A.-E., A.N., E.D., R.F., and A.C.-G. designed, discussed, and supervised the experiments. A.M. A.-E., A.N., E.D., and A.C.-G. provided experimental setups and resources necessary for this research. The first draft of the manuscript was prepared by J.Q. and A.C.-G. The final manuscript was written through contributions of all authors. All authors have given approval to the final version of the manuscript.

COMPETING INTERESTS

The authors declare no competing interests.

ADDITIONAL INFORMATION

Supplementary information The online version contains supplementary material available at <https://doi.org/10.1038/s41528-022-00157-9>.

Correspondence and requests for materials should be addressed to Jorge Quereda or Andres Castellanos-Gomez.

Reprints and permission information is available at <http://www.nature.com/reprints>

Publisher's note Springer Nature remains neutral with regard to jurisdictional claims in published maps and institutional affiliations.



Open Access This article is licensed under a Creative Commons Attribution 4.0 International License, which permits use, sharing, adaptation, distribution and reproduction in any medium or format, as long as you give appropriate credit to the original author(s) and the source, provide a link to the Creative Commons license, and indicate if changes were made. The images or other third party material in this article are included in the article's Creative Commons license, unless indicated otherwise in a credit line to the material. If material is not included in the article's Creative Commons license and your intended use is not permitted by statutory regulation or exceeds the permitted use, you will need to obtain permission directly from the copyright holder. To view a copy of this license, visit <http://creativecommons.org/licenses/by/4.0/>.

© The Author(s) 2022